



PAPER

# Waveform metrology: signal measurements in a modulated world

To cite this article: Paul D Hale *et al* 2018 *Metrologia* **55** S135

View the [article online](#) for updates and enhancements.

## Related content

- [Analysis for dynamic metrology](#)  
Andrew Dienstfrey and Paul D Hale
- [Optoelectronic time-domain characterization of a 100 GHz sampling oscilloscope](#)  
H Füser, S Eichstädt, K Baaske et al.
- [100 GHz pulse waveform measurement based on electro-optic sampling](#)  
Zhigang Feng, Kejia Zhao, Zhijun Yang et al.

# Waveform metrology: signal measurements in a modulated world

Paul D Hale<sup>✉</sup>, Dylan F Williams and Andrew Dienstfrey

National Institute of Standards and Technology, 325 Broadway, Boulder, CO 80305, United States of America

E-mail: [paul.hale@nist.gov](mailto:paul.hale@nist.gov)

Received 2 May 2018, revised 26 June 2018

Accepted for publication 6 July 2018

Published 3 August 2018



## Abstract

We review the waveform metrology program developed over many years at the National Institute of Standards and Technology. The goal of this program is to provide a measurement service capable of characterizing both temporal and frequency-domain instrumentation used with high-speed communication systems. Under our program, full waveforms as functions of both time and frequency are the target measurands. From these functional waveforms, traditional parametric descriptions can be derived. Furthermore, we give temporal waveforms and their frequency-domain representations consistent and equal consideration, with traceability to the International System of Units. To support this traceability, we emphasize voltage and current waveforms, their relationships, and the ability to transform both nominal values and their uncertainties from one domain to the other.

Keywords: covariance, impedance, waveform, electro-optic sampling, uncertainty, modulated signal, oscilloscope

(Some figures may appear in colour only in the online journal)

## 1. Introduction

The 1990s and early 2000s witnessed a period of explosive growth in consumer electronic items such as cellular telephones and personal computers. The high-performance networks used to connect these devices exploited new technologies in, for example, fiber optics, data servers, board-to-board interconnects, and power amplifiers. Over time, the bandwidth of these systems increased and the modulation formats employed became more complex. These high-speed systems were no longer high-budget products for elite customers. Rather, as consumer items, they needed to be manufactured economically and reproducibly. Standards, such as ITU-TS G.957 [1] and the IEEE 802.11 series of standards (starting with 802.11 – 1997 [2]), evolved to ensure that components from multiple vendors would be compatible. Consequently, measurements at higher bandwidths with tighter margins became paramount [3].

In response, researchers in academia and industry developed new measurement and instrumentation capabilities. Sampling-oscilloscope bandwidths increased from 20 GHz in

about 1988 to 50 GHz in 1991 and then 70 GHz in about 2002 [4]. Vector signal analyzers (VSAs) were developed to characterize the new complex modulation formats via the error vector magnitude (e.g. see [5] and other articles in that issue). Many of these instruments had the capability of measuring a signal in either the time or frequency domain.

As a particular example, consider the large signal network analyzer (LSNA)<sup>1</sup> designed to measure wave parameters under large-signal excitation [7]. Generally thought of as a frequency-domain instrument, the LSNA measures the magnitude and phase of waves scattered by a nonlinear device at the fundamental excitation frequency and at the harmonic and intermodulation frequencies. Like conventional vector network analyzers (VNAs), the LSNA must be calibrated to obtain the best results. In addition to the conventional VNA calibration standards [8], an LSNA must have a power calibration and a phase calibration that ties together the phase of the

<sup>1</sup> These instruments have been variously called vectorial nonlinear-network analyzers (VNNAs), nonlinear vector network analyzers (NVNAs), and large signal network analyzers (LSNAs). We refer to the instruments generically as LSNAs, with no reference to the hardware implementation or manufacturer [6].

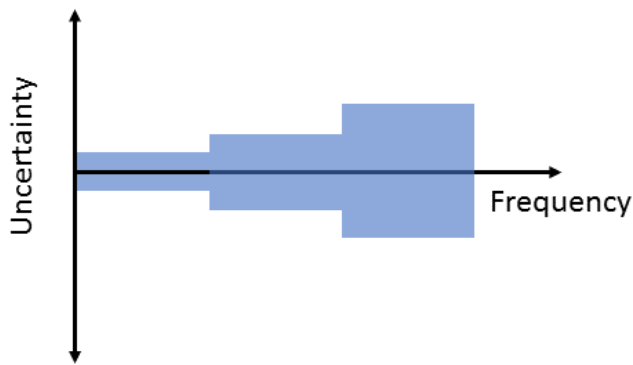


**Figure 1.** Typical frequency-domain instrument specification, which lacks correlation information and cannot be meaningfully transformed to the time domain.

fundamental to the phase at other frequencies<sup>2</sup>, allowing the results to be viewed in either the frequency or time domain.

Inspired by the work of Rush *et al* [10], Verspecht sought to calibrate the phase response of a harmonic phase reference (a comb generator) using an oscilloscope calibrated with the nose-to-nose method [11, 12]. In doing so, Verspecht found that errors in the oscilloscope calibration propagated into errors in his measurement of the comb generator response. Verspecht's work demonstrated innovative ways of estimating and then correcting errors due to the jitter [11, 13], timebase distortion [14], and impedance mismatch [11, 15]. While previous researchers had pointed to the existence of these errors and described some limited means to correct for them [16–18], Verspecht broke new ground in his attempts to account for all of them in a systematic way.

In seeking to calibrate the comb generator, and thereby the phase of the LSNA, Verspecht proposed a new traceability chain that included inputs from both time- and frequency-domain instrumentation. This created a problem in the metrology community as the time- and frequency-domain instrumentation of the day had separate traceability paths; the consistency of the two was by no means assured.

At the time, uncertainties in frequency domain measurements, such as those made by a power meter, spectrum analyzer, or VNA, were typically specified by the manufacturer in a table or graph similar to that shown in figure 1, where the vertical scale could represent uncertainty in either magnitude or phase. Specifications for instruments that were capable of both magnitude and phase measurements, such as VNAs, would include separate figures for magnitude and for phase. Critically, the functional variation of the uncertainty with frequency was unspecified and the relationship between magnitude errors and phase errors was unknown, making the

<sup>2</sup>The LSNA and its absolute calibration necessitated a new formalism, called wave parameters, that has revolutionized the way that microwave circuits are described, designed, and modeled. While scattering parameters [8, 9] are normalized by excitation wave magnitude and phase at each frequency, wave parameters are given in absolute magnitude, with the phase at all frequencies given relative to the phase of the incident fundamental wave. A discussion of wave parameters can be found in [7, 8] but is outside the scope of this review.

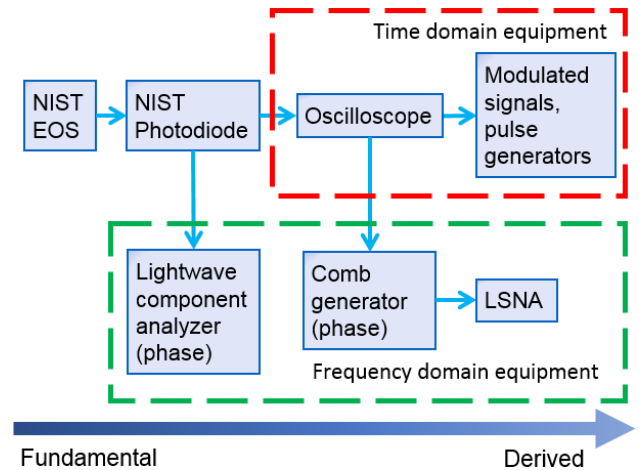


**Figure 2.** Notional diagram of NIST's traceability path for waveform metrology. The specific quantities that are traceable are listed in table 1.

transformation of frequency-domain uncertainties into time-domain uncertainties impossible.

Similarly, time-domain waveforms were specified in terms of a small number of pulse parameters [19] such as transition duration and pulse amplitude, and their uncertainties. In this case, heuristics based on assumed (but unverified) impulse- or step-response shape (i.e. Gaussian, exponential, Bessel-Thompson, etc), could be used to transform uncertainties in one domain to the other. These heuristics are often both quantitatively and qualitatively wrong, (see [20, 21]) and are not applicable to signals with complex modulations.

In this work, we review our approach to the development of a new and consistent waveform metrology infrastructure traceable to the International System of Units (SI). We emphasize that, although we say 'new', in some cases the techniques used were at least partially understood. We do, however, believe that we brought them together in a new, consistent, and unified way. We also attempt to place our work in the context of other contemporary researchers who greatly contributed to our thinking and apologize in advance for any oversights.

## 2. Consistent metrology infrastructure

In light of the above, we set out to develop traceability for modulated signals through a chain of calibrations involving opto-electronic transducers, oscilloscopes, and various waveform generators. This traceability path is shown schematically in figure 2. Key quantities that require traceability are outlined in table 1, with reference to the most relevant sections of this work and references that describe the necessary techniques. Of particular note, impedance and time traceability are required for each step.

With the trends of the time, we expected that the instrumentation using a measurement strategy in one domain might be used for applications in the other domain. Thus, we required that the traceability chain and uncertainty analysis

**Table 1.** Traceability to the SI for each step in figure 2, with method by which traceability is achieved and the most pertinent sections of this work and references where the method is discussed.

Quantity (SI unit)	Method (section, [reference])
EOS timebase (s)	Time calculated from stage position (meter) and speed of light (section 2.2.1, [22])
Power (W)	Power dissipated in load compared to DC power dissipated in resistor (section 2.2.1, [23–25])
Coaxial impedance ( $\Omega$ )	Impedance calculated from transmission line dimensions (meter) and impedance of free space (section 2.2.3, [8, 26–30])
On-wafer impedance ( $\Omega$ )	Impedance calculated from propagation constant (meter) and capacitance per unit length $C$ (farad/meter). $C$ calculated from DC impedance of resistor (ohm) and length (meter) (section 2.2.3, [31, 32])
Instrument timebase (s)	Directly traceable to NIST time standards (section 2.4.2, [33–39])

for time-domain instruments and frequency-domain instruments be consistent and equally valid in either domain.

Following the ideas of Gans [18], and inspired by the work of Verspecht [11–14], Cox *et al* [40], and Ridler [41], we introduced the concept of ‘full waveform metrology’ at the National Institute of Standards and Technology (NIST). Under this measurement paradigm, the waveform, and its functional form, is the target measurand from which parametric descriptions (e.g. transition duration, bandwidth, error vector magnitude) can be derived [20, 39, 42, 43]. Furthermore, we give temporal waveforms and their frequency-domain representations equal weight. We also emphasize the ability to transform both nominal values and their uncertainties from one domain to the other, simultaneously capturing both voltage and current waveforms, as well as their relationships in the description.

In more detail, full waveform metrology requires:

- (i) Calibration of units of time, frequency, and electrical and optical power.
- (ii) Calibration of the impedance of all components in the system.
- (iii) Calibration of the temporal impulse response or complex frequency response function of all measurement devices.
- (iv) Algorithms to account for impedance mismatch correction and finite bandwidth effects.
- (v) An unbroken chain of traceability and an uncertainty analysis linking each piece in the chain, capable of maintaining consistency while mapping between time- and frequency-domains.

We elaborate on each of these in the following:

### 2.1. SI-traceable response function

Several methods have been described for measuring the impulse response or complex frequency response of broadband sampling oscilloscopes [10–12, 15, 17, 18, 23, 44–58]. Broadly speaking these calibration methods fall into one of three categories: (1) swept-sine; (2) nose-to-nose; and (3) calibration with an ideal or known pulse source. The swept-sine calibration [15, 23, 49, 52] compares the amplitude of sine waves measured with the oscilloscope to the power of the sine waves measured with a calibrated power meter. This comparison determines the magnitude response of the oscilloscope at each frequency. The swept-sine calibration is traceable to the calibration of the power meter, and is the most accurate oscilloscope amplitude calibration currently available.

The main disadvantage of the swept-sine calibration method is that it cannot determine the phase of the oscilloscope frequency response, which is required for many microwave applications<sup>3</sup>. Without phase information, we cannot determine the impulse response of the oscilloscope in the time domain.

Switching attention to the temporal domain, when an oscilloscope is excited by a delta-function impulse from a source whose Thevenin-equivalent impedance is equal to the reference impedance, the waveform output by the oscilloscope is, by definition, the impulse response function. Unfortunately, such ideal pulse sources do not occur in practice and sources with sufficiently short duration (i.e. high bandwidth) to approximate a delta function have long been sought [17, 18, 44, 45, 51]. Frustrating this search, is the observation borne out over time that innovations either in signal generation or signal measurement are very quickly adopted by the other side. Therefore, in high-quality measurement contexts in which we measure the fastest signals using state-of-the-art devices, these two bandwidths are generally commensurate. It follows that other means of characterizing the impulse response of the highest-bandwidth oscilloscopes must be sought.

In 1990, a method that would eliminate the need for a known pulse was proposed [10]. This approach was based on the observation that certain sampling oscilloscopes produce a ‘kick-out’ pulse exiting the input port when the sampler is fired. Furthermore, some considerations suggested that this kick-out pulse would be proportional to the oscilloscope’s impulse response and could be used to estimate the oscilloscope’s impulse response. Using an ensemble of three samplers, we can use a strategy similar to the ‘three antenna method’ to estimate the impulse response of each particular sampler in the ensemble [52, 53, 56]. This technique came to be called the nose-to-nose method [11].

Upon closer inspection, verifying that the kick-out pulse was indeed proportional to the impulse response proved difficult. In fact, NIST researchers argued that the nonlinear capacitance of the sampling diodes made the kick-out pulse and impulse response differ at high frequencies [54, 60–62]. Thus, the situation was again unsatisfactory. An oscilloscope

<sup>3</sup> This is because the phase of the wave incident on the oscilloscope’s input port is unknown. We recently showed in [59] that an LSNA could be used to place a signal with a known phase (relative to the timebase reference and trigger signals) at the input port of the oscilloscope. However, the LSNA phase calibration is traceable through the oscilloscope calibration, and so cannot be used as an independent calibration of the oscilloscope’s phase response.

characterization method was needed that did not rely on a model of the pulse generator or the oscilloscope sampler's operation, and which could be soundly traced to other fundamental phenomena.

**2.1.1. Electro-optic sampling and SI traceability.** Whereas electrical generation of electrical impulses suffered from the commensurate bandwidth problems as discussed above, the same is not true for optical pulses. Mode-locked lasers can generate optical pulses with duration of 0.1 ps or less. When used in conjunction with ultrafast materials properties, these pulses can serve as the basis for generating electrical signals with bandwidths on the order of one terahertz or more. Thus, a new strategy emerges contingent on the ability to fully characterize optical to electrical conversion.

Several high-speed signal measurement methods based on photoconductive devices had been proposed since the mid 1970s (for a review, see [44, 45, 63, 64]). Photoconductive switches with response times in the picosecond and sub-picosecond regime can be used with a femtosecond laser 'probe pulse' to sample electrical signals or, in a different geometry, to generate electrical signals. However, the effects of parasitics in these devices are hard to fully characterize or model.

In contrast, electro-optic sampling [49, 65–67] can be used to noninvasively measure electrical signals and offers response times in the femtosecond regime<sup>4</sup> [65, 66] so that the effects of parasitics can be characterized and removed using microwave network analysis [71, 72]. Electro-optic sampling uses the linear electro-optic (Pockels) effect [73] that exists in certain crystals. When an electric field is applied to such a crystal, the optical retardance of the material changes differentially along the crystal axes such that a linearly-polarized optical beam propagating through the crystal will change its polarization state. This change can be detected using polarimetric methods. The result is a polarization measurement that is a linear function of the applied electric field [73, 74].

A schematic of our electro-optic sampling (EOS) system is shown in figure 3 [71, 75]. With this system, we can characterize a commercially-available photoreceiver as a portable electrical pulse source. The laser in figure 3 produces a periodic train of pulses with <100 fs duration in an open collimated beam. We split the laser pulses into two beams: an 'excitation' beam, and a 'sampling' beam, where the excitation beam excites the photoreceiver. When illuminated via its optical fiber input, the photoreceiver creates an electrical impulse at its coaxial output. Critically, as the duration of the optical excitation pulse is an order of magnitude shorter than the response time of the photoreceiver, the electrical signals generated by the photoreceiver are nearly equal to the receivers electrical impulse response. These electrical impulses propagate through the probe head and down to a coplanar waveguide (CPW) fabricated on an electro-optic wafer of LiTaO<sub>3</sub>.

It remains to measure this electrical signal using the electro-optic sampling strategy. The linearly-polarized sampling beam is passed through a variable optical delay, and then focused to a small spot at normal incidence to the surface of the LiTaO<sub>3</sub> wafer at the sampling reference plane of figure 3. The polarization of the emerging beam is then measured and inverted for electric field strength at this relative time instant. The full electrical waveform at discrete time instances is then measured by incrementing the relative delay between the excitation pulse and the probe pulse. The delay increments are set by changing the physical path length of the sampling beam. These path length increments are measured with a laser interferometer traceable to the SI [22]. The result is a vector of electrical field values sampled on a set of discrete, traceably calibrated, time instants that are nearly jitter free.

Typically, the change in polarization state is very small. To improve the signal-to-noise ratio, the optical excitation beam is chopped at a frequency of several kilohertz. The resulting modulation in the polarization state is measured by use of phase-sensitive detection and averaging while dwelling at each delay increment.

Due to the microwave impedance properties of the probe head, CPW, and CPW termination, the waveform that is measured at the sampling reference plane is distorted relative to the impulse emanating from the photoreceiver. Correction for the frequency-dependent impedance properties of the measurement system is accomplished by analysis of the circuit model shown at the bottom of figure 3. The impedances (or, equivalently, admittances) in this figure are determined by separate calibrations at the coaxial and the CPW reference planes. The procedure by which the measured signal is corrected is referred to as mismatch correction, and we will treat this in section 2.2.3. Once calibrated at the coaxial port, the photoreceiver can be disconnected from the EOS system and used as a known pulse source to calibrate oscilloscopes, lightwave component analyzers (LCAs), and other instruments that also have coaxial connectors.

There are a number of sources of uncertainty to be considered. After the impedance correction, effects due to the spatial extent over which the optical pulse and electric field overlap in the substrate become the next most significant error. Generally we can correct for this down to negligible levels up to at least several hundred gigahertz [60, 65, 72, 76] with a knowledge of the CPW dimensions and the substrate permittivity, thickness and refractive index.

The effects of multiple optical reflections can be reduced by application of an anti-reflection coating on the bottom of the substrate. The remaining errors created by this effect are estimated from the measured reflectivity of the substrate's bottom surface.

The small magnitude errors due to the temporal duration of the optical pulses, both in the excitation and in the sampling beams, can be traceably estimated by optical autocorrelation [77]. Phase errors due to the possibly non-symmetric shape of the laser pulse are negligible, based on fundamental mathematical arguments [65].

The EOS measurement system is quite linear with respect to the input voltage if the polarization measurement portion

<sup>4</sup> We note that one configuration for electro-optic sampling makes use of an electro-optic probe positioned slightly above the on-wafer circuit. Although this method has certain advantages, this method has been shown to invasively load the circuit [68–70]. See [67] for a review and comparison of different electro-optic sampling configurations.

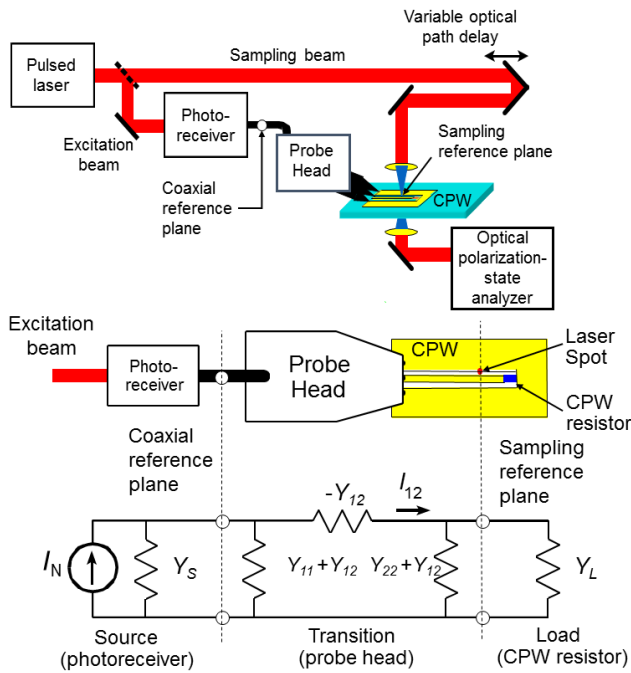


**Figure 3.** A schematic diagram of our electro-optic sampling system (top), a top-view schematic (center), and an electrical equivalent circuit (bottom). The photoreceiver generates a train of electrical impulses at the coaxial reference plane when it is excited by optical pulses at its input. These electrical impulses propagate through the probe head to the CPW on the electro-optic LiTaO<sub>3</sub> substrate, where they are sampled by the sampling beam. From [71, 75].

of the system is properly configured [73]. However, photoreceiver nonlinearity may be an issue, particularly when the photodiode is to be used for calibrating an LCA [78], where it is essential that the response of the photoreceiver to the sinusoidal stimulus in the LCA match the response to the short high intensity pulses of the EOS system. We prefer the use of a reverse-biased, side-coupled or waveguide-coupled PIN photodiode as the photoreceiver. These designs have a thin, but laterally distributed absorption region that achieves high bandwidth and efficiency while distributing the space charge that is the dominant cause of nonlinearity in these devices [79].

Unitraveling carrier designs [80] should be avoided because their bandwidth does not saturate monotonically with increasing input power, as shown in figure 4 of [81]. This particular mode of saturation causes significant discrepancies between the response to sinusoidal excitation and the Fourier transform of the response to impulsive excitation, even at low input powers. While PIN photodiodes also exhibit saturation at high powers, and this saturation can vary with the type of excitation [82], the power can be turned down to a level such that the error due to photodiode nonlinearity is substantially less than the other measurement errors.

Finally, the absolute scaling of the EOS measurement could be determined by comparison of the above measured signal with the signal measured when the system is excited with a square wave of known amplitude and frequency equal to the chopping frequency used in the measurement described above. However, we do not use this EOS-based scale factor

in practice. For one, it suffers from poor repeatability. Furthermore, when using this approach, we find that the resulting photoreceiver impulse response amplitude depends on the frequency of the calibration signals. We believe this arises due to a piezoelectric effect which couples optical propagation to crystal stress at acoustic frequencies, thereby complicating the absolute calibration of the field. Thus, the impulse response of the photoreceiver, as measured by the EOS system, is calibrated as a function of time with no units attached to the values of this function. In using the photoreceiver to calibrate oscilloscopes, we fix the overall scale of the oscilloscope response using a swept sine technique similar to that described in the appendix of [23]. The traceability of this last step is provided by a traceable power meter calibration from a few megahertz to a few gigahertz [24, 25]. Magnitude scaling for the LCA and LSNA can be provided by a traceable power meter, as described in [83] and [7], respectively. Improvements in the EOS-based scaling and swept-sine calibrations using modern equipment are subjects of on-going research at NIST.

### 2.2. Impedance traceable to the SI

The ‘signals’ in real high-frequency electrical circuits, systems, and instruments are most fundamentally described in terms of the time-varying electric and magnetic fields they generate. Practical, high-frequency system designs often incorporate single-mode waveguides because they are a low-loss method for transporting energy, in the form of electromagnetic waves, from one place to another inside the circuit and for coupling between systems. In single-mode waveguides, the waves can be described in terms of linear combinations of forward and backward propagating modal solutions to Maxwell’s equations [8, 84, 85]. These waves, and the impedances that set their boundary conditions, are essential to waveform metrology and microwave measurements in general. We emphasize that we cannot fully describe the interactions between two microwave circuits, systems, or instruments with a single signal. Both voltage and current waves, or linear combinations of them, must be specified, and therefore, the circuit impedance must be accounted for.

At high frequencies, it becomes difficult if not impossible to accurately design an electrical circuit to have a nearly ideal, or even a specified, electrical impedance. This is because even small imperfections in the circuits lead to complicated changes in impedance which cause difficult-to-predict effects including losses, distortion, and multiple reflections that arise when transferring a signal from one device to another.

For example, consider the impedance of an oscilloscope. When the oscilloscope’s input impedance is matched to 50 Ω, the reflection coefficient is low and energy is efficiently coupled into the oscilloscope. If the reflection coefficient is high, the internal circuitry of the oscilloscope does not ‘see’ the incident wave because a large portion of the incident wave is reflected. Typically, we want to design the oscilloscope’s impedance to have a low reflection coefficient at all relevant frequencies such that the reflection does not distort the measured signal.

Figure 4 shows the impedance of three identically-manufactured equivalent-time oscilloscopes and the variation between them. Here, ignoring the complex nature of the impedance, we see that the oscilloscope impedances are not well matched to  $50\ \Omega$ , and their impedances are quite different from each other. Thus, the impedances of these oscilloscopes, and most microwave instruments, for that matter, must be individually measured and accounted for, particularly at high frequencies.

For purposes of metrology, we can measure the wave incident on an oscilloscope having an arbitrary (but known) impedance and then calculate the wave that the generator would deliver to a perfect load. This calculation is called mismatch correction. Also, when a wave is measured at one end of an adapter, transmission line, or other fixture, we can use the measured fixture transmission and reflection properties, as well as the generator and oscilloscope impedances, to calculate the wave at the input end of the fixture. This calculation is called de-embedding.

In the late 1990s, mismatch corrections and de-embedding were well known and commonly used by microwave engineers [9, 86], and were also not new in the field of waveform metrology [17]. But still, many of those in the time-domain community were unfamiliar with these techniques for accounting for source, load, and interconnect impedance mismatch, and no national metrology institute (NMI) had established a mismatch-corrected traceability path for sampling oscilloscopes [47, 48, 50, 87]. In the course of developing a more rigorous traceability path for optical receivers, oscilloscopes, waveform generators, and the LSNA, we had to grapple with impedance in the context of optoelectronic devices [78, 83] and particularly in the context of time/frequency-domain transformations [15, 71, 88–91].

In sections 2.1.1 and 2.2.2, we use the particular example of EOS to illustrate why impedance effects such as the termination impedance are important in waveform metrology and why the traditional approach of time-gating is insufficient to address the problem. Then, in section 2.2.3 we show the results of de-embedding in the EOS measurements to obtain an equivalent circuit representation of the photoreceiver at its coaxial output port.

**2.2.1. Application to EOS.** The circuit of the EOS system is shown in the middle and bottom of figure 3. Here the photoreceiver on the left generates the electrical pulse that propagates down a section of CPW printed on the  $\text{LiTaO}_3$  wafer, before it arrives at the location in the CPW where the voltage is measured. The electrical pulse then continues propagating down the CPW until it reaches the CPW termination resistor.

The photoreceiver and probe contain significant lengths of transmission line that add to the lengths of CPW in the circuit. Put all together, these transmission lines introduce over 250 ps of delay between the photoreceiver and the resistor.

In order to demonstrate the effect of the circuit termination, we terminated the CPW in figure 3 in two different ways. Figure 5 shows the temporal measurements with each of the terminations. When the CPW was terminated with a  $34.8\ \Omega$  resistor the electro-optic sampling system measured a solitary pulse at about 180 ps, shown in black. However, when

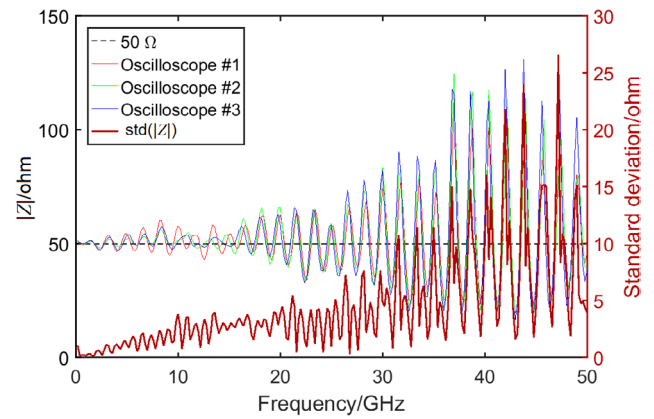


**Figure 4.** Magnitude of the impedance of three 50 GHz bandwidth oscilloscopes. The sample standard deviation of the three values is also shown, giving an indication of the spread in values.

the resistor was replaced with an open circuit, the red dashed curve was measured. Here, a much larger main pulse at 180 ps, and a series of additional pulses at 750 ps, 1400 ps, and 2000 ps are plainly visible. These additional pulses are due to the voltage pulse from the photoreceiver reflecting off the end of the CPW transmission line, and then making several round trips between the end of the CPW and the photoreceiver. Even when the CPW is terminated with a resistor, as we would normally do in practice, small but visible multiple reflections are still present at 750 ps, 1400 ps, and 2000 ps.

**2.2.2. Time gating.** Time gating is a traditional approach, often used by the time-domain community, to handle multiple reflections. In this approach, the temporal measurements of figure 5 would be truncated somewhere between 600 ps and 700 ps.

However, the first pulses measured at 200 ps in figure 5 are completely different, even though the same photoreceiver, probe, and electro-optic sampling system were used in both cases. This is because the resistor and open are located slightly to the right of the sampling reference plane shown in figure 3. Thus, the reverse traveling pulse, reflected off the resistor and open, is slightly delayed in time but overlaps temporally with the forward traveling pulse.

Because the impedance of the CPW resistor is lower than the impedance of the source<sup>5</sup>, the pulse reflected by the resistor is distorted and inverted. The superposition of forward and backward traveling pulses results in a distorted measured pulse, with decreased amplitude and sharpened falling edge. However, because the impedance of the CPW open is higher than the source impedance, the reflected pulse is distorted but not inverted. Here the superposition of forward and backward traveling pulses results in a distorted pulse measurement that is broadened and of higher amplitude than the incident pulse from the photoreceiver.

Our conclusion is simple: neither truncated result is correct. While the experiment might have been reconfigured to make the temporal overlap between forward and backward

<sup>5</sup> Note that in this context, the source is everything to the left of the measurement plane in figure 3 and the termination is everything to the right of the measurement plane.

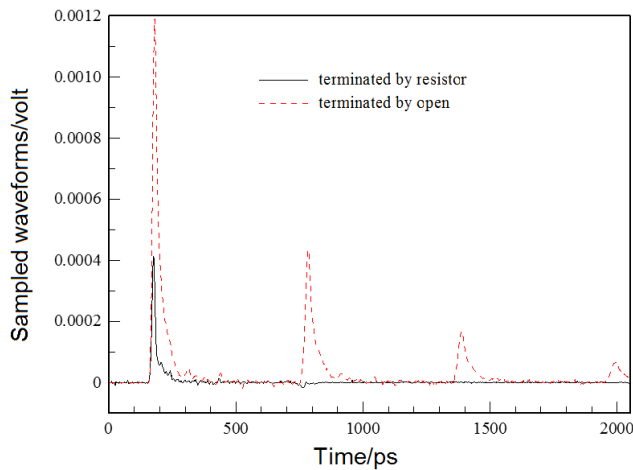


**Figure 5.** Two waveforms measured by our electro-optic sampling system. The solid line corresponds to a measurement with the CPW terminated by a  $34.8 \Omega$  resistor, and the dashed red line corresponds to a measurement with the CPW terminated by an open circuit. Except for these terminations, all of the conditions in the experiment were identical. From [71, 75].

traveling pulses less, the duration of the windowed waveform is subjective. Ambiguity in when the forward traveling pulse ends and when the reverse traveling pulse begins could lead to uncontrolled uncertainty<sup>6</sup>. Furthermore, neither of the above procedures accounts for the frequency-dependant loss of the probe, the probe-to-CPW interface, or the CPW. Rather, all of the impedances and transitions in the system must be characterized and accounted for systematically with a method that applies to signal measurement problems broadly. Microwave circuit theory gives us a path forward.

**2.2.3. Mismatch correction.** We now see clearly that losses and the impedance of the termination at the end of the CPW transmission line must be corrected for if the impulse response of the photoreceiver, which is a property of only the photoreceiver and not the measurement system, is to be determined from the measurements. Doing this requires measuring the circuit parameters of the lower circuit of figure 3 in the frequency domain by use of a VNA and then Fourier transforming the voltage at the measurement reference plane for analysis in the frequency domain.

As described in [71], we must first calibrate the VNA at a coaxial reference plane using coaxial calibration standards [8] and measure the reflection coefficient of the photoreceiver. Traceability for this calibration is derived from mechanical measurements of the transmission-lines that are used for calibrating the VNA. The impedance of these transmission lines is directly calculable from their geometry and the low loss of the metals used [26–30]. Traceability for other coaxial VNA measurements in our traceability path is assured in the same way.

We then perform a second-tier multiline thru-reflect-line calibration directly at the sampling reference plane in the CPW using standards that are fabricated on the  $\text{LiTaO}_3$  wafer

<sup>6</sup>For an example of a pulse with echo-like components that could mistakenly be windowed, see [88].

itself. This calibration is based on direct broadband measurements of the traveling waves in the CPW [8], and avoids errors inherent in on-wafer short-open-load-thru calibrations [92].

Traceability for the CPW calibration is derived by estimating the characteristic impedance of the CPW from the propagation constant of the transmission lines, which is determined directly by the thru-reflect-line calibration and measurements of the length of the CPW lines employed. We calculate the characteristic impedance of the CPW using the method of [31] based on the constant-capacitance approximation [32], which are consistent with the causality and power conditions of [8, 84]. In our implementation, the capacitance is determined at low frequency from a measurement of a small embedded resistor with known DC resistance, and extrapolated to high frequencies through a knowledge of the properties of the dielectrics employed in the CPW, as described in [32]. Finally, we set the reference impedance to  $50 \Omega$  using the method of [31], which completes the calibration process.

We measured the reflection coefficient  $\Gamma_L$  of the CPW terminations using this calibration, and determined the scattering parameters of the probe head, which were equal to the ‘error boxes’ determined by the second tier TRL calibration. As shown in [76], these scattering parameter measurements are all traceable to fundamental physical measurements or standards.

Uncertainty analysis of on-wafer measurements has evolved over time, and includes the analytic work of [93], different methods for propagating the calibration uncertainties into the measured quantities, as in [94, 95], and accounting for the effects of cross-talk between probes, as in [96]. Traceability of on-wafer measurements continues to evolve, for example, through various European Metrology Programme for Innovation and Research (EMPIR) Projects [97–100].

Once we determined the electrical reflection coefficients of the photoreceiver and the CPW load, and the scattering parameters of the probe head, we determined the admittances  $Y_s$  of the photoreceiver and  $Y_L$  of the CPW load, and the admittance parameters  $Y_{ij}$  of the probe head, using standard transformations [8]. Finally, we constructed the equivalent circuit shown in figure 3, which is based on these measured quantities and de-embed the measured voltage to determine an equivalent circuit representation of the photoreceiver.

Figure 6 shows how effective these corrections can be. The figure shows the photoreceiver’s frequency response magnitude calculated from these two measurements both before and after de-embedding. After de-embedding the two dissimilar measurements are in good agreement. The frequency response phase, not shown here, but necessary for our applications, is also in good agreement.

The de-embedded result is only rigorously determined in the frequency range over which the *coaxial connector* supports single-mode operation. Although the plots shown here for demonstration purposes extend only up to 40 GHz, the above strategies have been used up to 110 GHz [74], and higher frequencies can be reached with the newer 1.0mm connectors that are single mode up to 120 GHz or 0.8mm connectors that are single mode up to 145 GHz.

Extension of our method to frequencies beyond the coaxial-waveguide single-mode cutoff requires assumptions about the

high-order modes and their termination impedance that may be difficult to rigorously verify. If all the significant energy in the complex frequency response function is captured below the single-mode cutoff frequency, the response function can be Fourier transformed to obtain the temporal impulse response.

Alternatively, a filtered version of the time-domain impulse response can be obtained by setting the frequency response above the single-mode cut off to zero and Fourier transforming back to the time domain. Sinc-function like artifacts due to this hard cutoff will be more or less visible, depending on the fraction of the energy that was dropped by the filter.

Removing the coaxial waveguides from the measurement problem and moving to a fully on-wafer measurement configuration may significantly extend the frequency range over which mismatch corrections might be applied. However, on-wafer waveguides can still have multiple propagating modes, both guided and radiated, that must be considered. Applications of fully on-wafer measurements are discussed section 3.1.

In closing this section on impedance in waveform metrology, we note that the group at Physikalisch-Technische Bundesanstalt (PTB) [20, 48, 58, 72, 100, 101] has developed a more time-domain-centric approach to characterizing impedance and correcting for its effects. Application of this approach to determining reflection and transmission coefficients, along with comparison to measurements performed with a frequency-domain VNA, are described in [100]. Calibration of a photoreceiver pulse source with this strategy is described in [101]. A round robin comparison of photoreceiver measurements performed at several NMIs is currently underway [102].

### 2.3. Finite bandwidth effects

In section 2.1 we discussed how oscilloscopes have been calibrated in the past and described the approach we took, based on EOS. In this section, we discuss the signal estimation and instrument calibration problems from a mathematical perspective. Consider the example of using an oscilloscope to measure a short-duration, impulse-like waveform. Ideally the output trace of the oscilloscope would identically match the electrical input. While this is true for slow signals, for faster signals we find that the oscilloscope trace, considered as is, is not a good estimate of the input. First there may be a small delay between when the impulse arrives and when the oscilloscope trace indicates this event. Furthermore, whereas the input signal may return to zero as abruptly as it began, the oscilloscope trace generally exhibits damped oscillations at the tail end of the pulse before eventually returning to zero. Both features are manifestations of the physical fact that, despite considerable engineering efforts invested in the oscilloscope's design, the microwave circuits still have inertial-like characteristics based on Maxwell's equations and the dynamics of charge.

Note that the terms 'slow' and 'fast' appearing in this discussion do not refer to absolute time scales. Rather, the issue is the rate of modulation of the input signal relative to the rate at which the oscilloscope can respond. In practice these

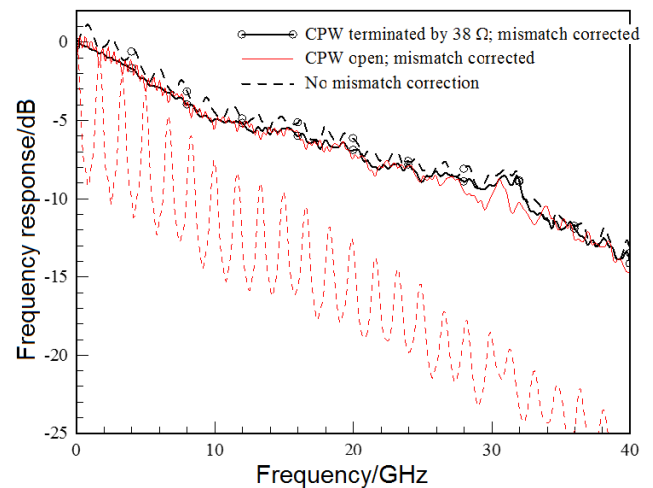


**Figure 6.** A comparison of the corrected power spectrums of  $V_{50}$  for the two waveforms shown in figure 5. The uncorrected spectrums of  $V_e$  are shown in dashed lines. The curves are normalized to 0 dB at DC. From [71, 75].

rates are indicated by the bandwidth specification of both signal and oscilloscope. For example, a modern microwave sampling oscilloscope might be characterized as having a 100 GHz bandwidth. Such an oscilloscope would introduce relatively little distortion of an input signal with characteristic frequency content restricted to tens of megahertz. By contrast, quantitative distortions are expected when measuring microwave signals with bandwidths on the order of tens of gigahertz. The fact that the oscilloscope waveform cannot be taken as a direct estimate of the underlying signal is referred to as a 'finite bandwidth effect'. We discuss this formalism and our correction procedures in more detail below.

**2.3.1. Deconvolution and regularization.** We model our measurement devices as linear, time-invariant (LTI) systems. Such systems are characterized by their impulse response function which we denote by  $h(t)$ . Conceptually,  $h(t)$  is the trace that would result if the oscilloscope received a delta function at its input. More generally, if we consider the input as a sum of delta functions with strengths  $x_j$  and originating at times  $s_j$ , then for any measurement time  $t$ , the oscilloscope waveform,  $y(t)$  would be the sum of response functions scaled by  $x_j$  and shifted in time by  $s_j$ . In other words,  $y(t) = \sum_j x_j h(t - s_j)$ . In the event that the input is a continuous function, then the sum may be replaced by an integral. Thus, informally, we have derived the result that the output of an LTI system is given by the convolution of the input with the system response,

$$y(t) = \int_{-\infty}^t x(s)h(t-s)ds. \quad (1)$$

In the context of LTI systems the two most common experimental tasks are calibration and input estimation. In the former, the goal is to excite the measurement system in such a way as to estimate  $h(t)$ , the response function. This can be done in either the time- or frequency-domain. Referring to the discussion above, use of the EOS system to determine the photoreceiver's response function is an example of a time-domain calibration, whereas the swept-sine calibration

of an oscilloscope's response function is a partial solution to the frequency-domain calibration problem. Note that in the calibration experiment, the researcher has flexibility to fix the input waveform,  $x(t)$ , in order to have desired characteristics.

The estimation problem may be stated as follows: Given a waveform  $y(t)$ , as measured on a calibrated system with impulse response function  $h(t)$ , what is the best estimate of the input signal  $x(t)$ ? Mathematically this estimation problem is referred to as deconvolution. Whereas in principal, we could discretize the integral in (1) and attempt to solve the problem directly in the time-domain, we can better perform and analyze deconvolution algorithms in the frequency-domain.

Fourier analysis is a subject unto its own. We recommend [103] for mathematical treatment motivated by engineering applications. For our purposes here, the critical element of this theory is the Fourier Convolution Theorem relating convolution in the time-domain to multiplication in the frequency-domain. Mathematically, we have

$$y(t) = \int_{-\infty}^{\infty} h(t-s)x(s)ds, \text{ if and only if} \quad (2)$$

$$Y(f) = H(f) \cdot X(f). \quad (3)$$

Here the capitalized functions are the Fourier transforms of their lower-case counterparts.

The Convolution Theorem suggests that the deconvolution problem can be solved by division. Given a response function  $h(t)$  and a measured signal  $y(t)$ , upon computing the Fourier transform of both, we may simply estimate the Fourier transform of the input signal as

$$X(f) = \frac{Y(f)}{H(f)}. \quad (4)$$

The time domain signal  $x(t)$  is computed from the inverse Fourier transform.

While this procedure is fine in theory, in practice two issues emerge. The first is that, the denominator in (4) tends to zero at large frequencies; i.e.  $|H(f-f_0)| \rightarrow 0$  as  $|f-f_0| \rightarrow \infty$ . Physically, this corresponds to the fact that, for sufficiently large offsets from the instrument's intended frequency range, the device will simply not respond and the measurement at that frequency will be zero. Presumably the energy of the input is either scattered back out of the instrument or dissipated into heat. The second issue pertains to measurement uncertainty and noise. As is well-appreciated by readers here, all measurements contain an associated uncertainty. Furthermore, we generally expect that uncertainty, or 'noise' energy, distributes broadly across frequencies; for example, the spectrum of 'white noise' is flat.

The combination of these two features—small denominator arising from physical/mathematical considerations, and non-zero numerator due to measurement effects—results in the well-known fact that this division algorithm is unstable. If executing it as suggested above, there will be frequency regions in which modest noise energy is amplified by a large factor corresponding to the reciprocal of  $H(f)$ . Whereas these regions are localized in the frequency domain, the

time-domain estimates of  $x(t)$  exhibit erratic and extremely large oscillations throughout the measurement window and are thereby useless. More careful analysis is required.

Despite the instabilities alluded to above, the deconvolution problem is not entirely hopeless. The idea is that there is a region in the frequency-domain in which both the system response function and the signal-to-noise ratio are sufficiently large such that the division can be performed with confidence. Thus the goal is to monitor the high-frequency decay of the response function alongside the emergence of a 'noise-floor' in the spectrum of the measured signal; i.e.  $|H(f)|$  in relation to  $|Y(f)|$ . Outside of some frequency range, this division should cease and the estimate  $X_\lambda(f)$  extended by other considerations. Here we have introduced the  $\lambda$  subscript to indicate that the inversion algorithm performs the division over a frequency region that is effectively tuned by this parameter. In the simplest case, the extension can be by zero as in  $X_\lambda(f) = 0$  for  $|f-f_0| > f_\lambda$ . More elaborate possibilities can also be utilized. In any case, the goal is to provide a reliable estimate,  $X_\lambda(f) \approx X(f)$ , in such a way as to be stable in the presence of (unavoidable) measurement uncertainty. Mathematically, the instability of deconvolution corresponds to the statement that deconvolution is an ill-posed problem. Techniques for stabilization of the inversion come from the study of regularization theory for the inversion of ill-posed problems. This theory is overly technical for presentation here; see [104–106] for more details.

#### 2.4. Timebase traceable to the SI

Waveforms are a record of a physical phenomena as a function of time [19]. Likewise, the Fourier transform of the waveform is a function of frequency. In order for the waveform, measured in the time or frequency domain, to be totally traceable to the SI, the time axis or frequency axis must be traceably calibrated. We have already discussed, briefly, calibration of the time scale of the EOS system, traceable to the SI through the laser interferometer wavelength and the speed of light. In this section, we focus on the timing errors in equivalent-time (sampling) oscilloscopes, which are similar for all manufacturers. Real-time oscilloscopes are a different matter entirely. See [107] and section 3.3 for a discussion of the differences between these two types of oscilloscopes.

**2.4.1. Timing errors in equivalent-time oscilloscopes.** In the following two sections, we discuss only equivalent-time oscilloscopes and, for brevity, refer to them simply as oscilloscopes. Timing errors in oscilloscopes are generally broken into three categories. Systematic errors, called timebase distortion, are repeatable over a short period of time from measurement to measurement, as long as the sample interval and waveform epoch are kept fixed<sup>7</sup>. Timebase distortion can include a linear compression or stretch of time scale, as well

<sup>7</sup> From [19], the *waveform epoch* is defined as 'An interval to which consideration of a waveform is restricted for a particular calculation, procedure, or discussion. Except when otherwise specified, this is assumed to be the span over which the waveform is measured or defined'.

as nonlinearities in the time scale. Jitter is an error that varies randomly from sample to sample within a single waveform measurement. These random variations are usually modelled as uncorrelated between samples, but correlated errors are possible. Drift is a correlated shift of the waveform within a single measurement epoch, which can change randomly from measurement to measurement.

The oscilloscope, without timing errors, measures the waveform at evenly-spaced time intervals. However, when timing errors are accounted for, the samples occur at varying intervals, sometimes jumping forward in time and sometimes jumping backwards. As an extreme example, the averaged impulse measurement in figure 7 exhibits a time discontinuity on the rising edge. Samples on the right of the discontinuity were actually measured at an earlier equivalent time than the samples just to the left of the discontinuity. This and similar errors violate our assumption of time invariance and must be corrected before correcting for impedance effects and before deconvolution.

**2.4.2. Correcting timebase errors.** Considerable research was conducted on estimating and correcting timing errors in oscilloscopes throughout the 1990s and early 2000s, by us and several other groups; for example, see [14, 34–36, 108–111]. Eventually, commercial solutions were developed to estimate and correct timebase distortion and jitter down to roughly the 200 fs level. Recent oscilloscope implementations may reduce timebase errors even further.

At NIST, we implemented a method, for traceably correcting timebase distortion and jitter in some oscilloscopes, that we call the timebase correction (TBC) algorithm [34–36]. A similar technique was also developed at the National Physical Laboratory in the United Kingdom [111]. Typical measurement apparatus for TBC is shown in figure 8. Here, the waveform generator (under test) and the trigger signal are all synchronized with a local oscillator (LO). This LO is, in turn, referenced to an SI traceable clock, such as one of the NIST Hydrogen masers [33]. This technique can be used both when calibrating the oscilloscope [112] and when using the oscilloscope to calibrate various waveform generators, such as in [37–39].

The idea is that we ultimately reference the measurement time of each sample of the signal of interest to the traceable LO. In the apparatus, each time the oscilloscope is triggered, all of the samplers in the mainframe are fired simultaneously from a single strobe pulse generated by the oscilloscope's timebase. When the samplers are fired, any errors in the timebase, either systematic or random, are reflected in the measurements performed by each sampler. This means that the timing errors in the measured quadrature LO sinusoids on channels 1 and 2 are indicative of the timing errors in the channels 3 (and higher) that are used to measure the signal(s) of interest. Note that because the LO sinusoids are approximately  $90^\circ$  out of phase, one of the sinusoids always has a non-zero slope and is therefore sensitive to timing errors.

The uncorrected timebase of the oscilloscope gives an initial estimate of the time for each sample. This estimate is then refined by fitting the LO sinusoids with an orthogonal distance regression algorithm. Finally, the fit residuals in

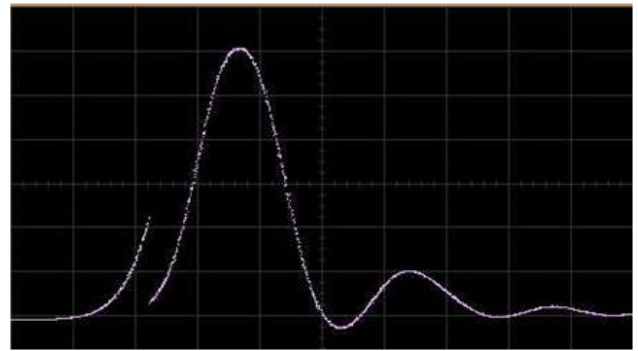


**Figure 7.** Measured impulse positioned on a timebase discontinuity. Timebase distortion often includes, but is not limited to such discontinuities. The measurement has been averaged to reduce the visible effects of random processes such as jitter and additive noise.

the horizontal direction are then used to calibrate the time at which each sample was taken. Because the samplers impart their own timing and voltage noise, the lowest achievable jitter after TBC is limited to about 200 fs.

When averaging, drift effects, such as differing thermal expansion between the path traveled by the signal of interest and the LO sinusoids measured on channels 1 and 2, can significantly impact the measurements. Several drift estimation algorithms that are applicable to impulse-like waveforms are described in the literature; for example, see [113–115] and references therein. A method for aligning band-limited modulated signal measurements is described in [116].

### 2.5. Uncertainty analysis

Systematic errors generally have structure, and that structure changes as the error is transformed to another domain. For example, multiple reflections in and between mismatched electrical circuits can be thought of as echoes. When an impulse travels through a circuit, the output is often a train of decaying pulses. These decaying pulse trains in the time domain correspond to characteristic ripples in the frequency-domain scattering parameters.

Figure 9 from [89] illustrates the temporal voltage of a photoreceiver measured on our electro-optic sampling system in (black). The electrical pulse generated by the photoreceiver reaches a peak of nearly  $3.5\text{V/pC}$  at about 40 ps. This pulse was calculated from the inverse Fourier Transform of the photoreceiver's frequency response, zeroed out above 110 GHz. We also see the first round-trip reflection between the photoreceiver and the CPW resistor at about 400 ps. Most of this round-trip reflection has been removed by the mismatch corrections, but some residual vestiges of the reflection can still be seen there.

Figure 9 also shows the uncertainties in this measurement calculated in two different ways. The red dashed curve shows the uncertainty from our correlated uncertainty analysis. As expected, uncertainty peaks near 40 ps where the signal reaches a maximum. That is, uncertainties in the measurements are small before the pulse arrives, grow larger when the pulse arrives, and then slowly get smaller after the pulse stops.

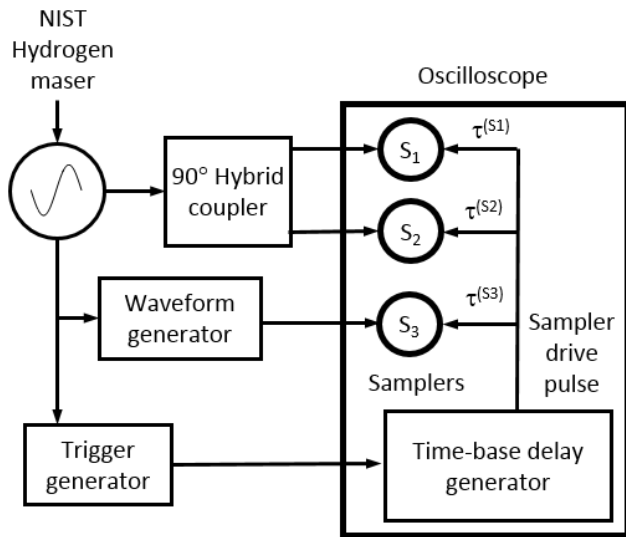


**Figure 8.** Apparatus used to calibrate the timebase of some equivalent-time oscilloscopes by use of the timebase correction (TBC) algorithm. In this system, the timing errors  $\tau$  in channels (samplers) 1, 2, and 3 are highly correlated. The TBC algorithm uses orthogonal distance regression to fit the quadrature sinusoids measured on channels 1 and 2. Horizontal residuals in this fit are then used to calibrate the oscilloscope’s timebase.

Finally, we see the uncertainty rise slightly near 400 ps, where the imperfect mismatch correction was applied to try to remove the multiple reflections in the system. These uncertainties are all consistent with our understanding of the measurement system.

The blue dashed curve (marked with circles) shows the result of an uncertainty analysis that ignores correlations. Here the uncertainty level is uniform, even long before the pulse arrives, and after the pulse has ended. The uncertainty does not grow where the signal reaches a peak and the uncertainties do not track known imperfections in the mismatch and other corrections. This is because, without any information on the correlations in the frequency domain, the error must be treated as uncorrelated white noise. Uncorrelated noise in the frequency domain translates into noise that is uniformly distributed over time. Clearly, neglecting the correlations in the uncertainty loses several important aspects of the uncertainty.

**2.5.1. Consistent uncertainty analysis in the time and frequency domains.** Oscilloscopes and the electro-optic sampling system are temporal systems, while the vector network analyzers we use to characterize the mismatch in these systems are frequency-domain systems. As a result, our measurement strategy has forced us to continually transform from one domain to the other [38, 71, 91]. We not only needed to transform our measured results from one domain to the other, but we were confronted with the need to transform our uncertainties between the time and frequency domains as well. However, we could not do so without knowing how they were correlated.

From the example above, uniform noise in one domain propagates to uniform, un-correlated noise in the other domain. However, the residual error in our mismatch correction has

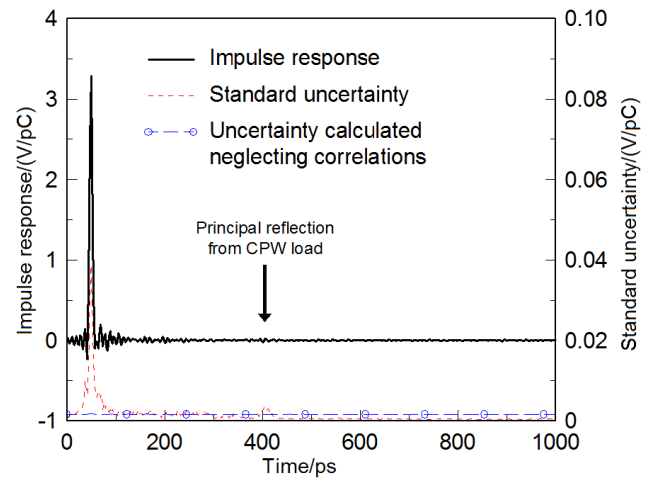


**Figure 9.** The measured temporal voltage that a photoreceiver generates across a perfect  $50 \Omega$  load when the photoreceiver is excited by a short optical pulse that generates a picocoulomb of charge at its bias port, and its standard uncertainty after correction, from [89].

generally resulted from imperfections in our measurement equipment and calibration artifacts that were also due to mismatch. Thus, they were characterized by highly-correlated ripples in the frequency domain, and highly correlated decaying pulse trains in the time domain. This also required us to understand and account for the correlations in our uncertainty of our mismatch corrections before applying the Fourier transform.

**2.5.2. The microwave uncertainty framework.** We developed an uncertainty analysis software tool [95] to automatically track the correlations in our measurement uncertainties as we propagated them through Fourier Transforms and other complex calibrations and data processing steps. This tool is designed to handle correlated uncertainties in large correlated vectors, as well as correlations introduced by reusing calibration artifacts or error mechanisms in different parts of the procedure.

The vectors are typically functions of time or frequency, but may be functions of other variables as well. Each element in these vectors can be a scalar, a complex number, a vector of scalars or complex numbers, or matrices of scalars or complex numbers. Common examples include temporal waveforms, which are functions of time, and complex scattering-parameter matrices, which are functions of frequency.

**2.5.3. Sensitivity analysis.** In our software tool [95] we assign unique names to each error mechanism to track reuse of calibration artifacts or error mechanisms. The tool stores nominal values of the vectors it is designed to treat, as well as a perturbed vector corresponding to the results of a sensitivity analysis for each error mechanism in the problem. Each of these perturbed vectors corresponds to the results of the analysis performed when each of the error sources in the problem is turned off except for one, which is identified by its unique name.

We calculate these sensitivities with a simple forward-difference method, using a step size equal to the standard

uncertainty of the error mechanism in question. While this is not extremely efficient from a numerical point of view, the method offers a straight-forward and robust way to perform the sensitivity analysis. As each result is a perturbed version of the nominal vector, correlations in the uncertainties are preserved. However, like all sensitivity analyses, the transformations that are applied to the data must be linear.

**2.5.4. Monte-Carlo uncertainty analysis.** Monte-Carlo analysis can be used to calculate the uncertainty of both linear and nonlinear problems, and to determine the probability density functions of its results. This is accomplished in the distributed calculations supported in our software tool by locally generating Monte-Carlo results based on the names assigned to each error mechanism in a deterministic way.

The Monte-Carlo analysis can be used not only to identify probability distribution functions, but to identify systematic bias in nominal results created by nonlinearity in the calibrations and processing steps. Systematic bias is a common occurrence, as many physical phenomena in the calibrations and processing steps are nonlinear.

Figure 10 illustrates the importance of Monte-Carlo analysis. The figure shows a histogram of the magnitude of the transfer function  $S_{21}$  of a passive junction between a rectangular waveguide test port and a passive calibration standard. This transfer function cannot be greater than one because the connection is passive, and cannot create energy. Thus, any deviation from a perfectly aligned junction either does not change the magnitude of the transfer function, or reduces it.

In this case, the best estimate of the electrical behavior of the junction is that it is perfectly aligned, in which case the magnitude of  $S_{21}$  is equal to one (i.e. 0 dB). This nominal value of the magnitude of  $S_{21}$  is denoted by the red line on the plot at 0 dB.

The Gaussian distribution plotted in green in figure 10 is the estimate of the probability distribution function from the sensitivity analysis, and is centered on the red line at 0 dB. However, we know that the actual value of the magnitude of the transfer function cannot exceed one, as the Gaussian distribution calculated from the sensitivity analysis might lead us to believe. Thus, we see that the Gaussian distribution assumed in our sensitivity analysis cannot be correct.

The distribution of the Monte-Carlo estimates is shown in figure 10 in black with crosses, denoting the maximum number of occurrences in each histogram bin. Here we see that the probability density function is always less than one (0 dB), as we expect. The blue line marks the average of the Monte-Carlo estimates, and represents our best estimate of the average value of the transmission through the junction.

### 3. The future of waveform metrology

The full waveform metrology paradigm has provided a solid foundation for traceable modulated signal measurements (e.g. see [39]). As depicted in figure 2, this foundation includes traceability to the SI through electro-optic sampling, RF

power metrology, traceable time scales, and traceable impedance standards.

In addition, electro-optic sampling is now accepted as the preferred method for providing traceability for LSNA phase, oscilloscope response, and lightwave component analyzer phase [20, 62, 78, 101, 102, 117–121].

Each step in the traceability chain can now be made consistent between the time and frequency domains and connected by an uncertainty analysis that is equally valid in both domains. Uncertainty analyses similar to those presented here, that track uncertainty correlations, and which support a consistent analysis in the time and frequency domains are now being pursued by academia, industry, and other NMIs [20, 101, 115, 122–126] both for high-speed waveform measurements and for lower-speed force, pressure, and acoustic measurement systems. To the best of our knowledge, none of these analyses or tools integrate Monte-Carlo analysis and the ability to cascade calibration uncertainties through many steps, e.g. from the EOS and VNA measurements, through and oscilloscope calibration, and into waveform generator calibration. However, the field is quickly evolving and other advanced tools may soon be available. Frequency-domain tools for VNA uncertainty analysis are also quickly evolving [127–129] and may soon integrate time-domain capability, Monte-Carlo analysis, and extension beyond s-parameter measurements.

Full waveform uncertainties are proving to be valuable in their own right [124, 130–132]. For example, in [131] the step-responses of high-speed HBT transistors were measured and also modelled with an industry standard transistor modeling software package. The measurement uncertainties and process variations were propagated through the integrated circuit design process, allowing designers to assess the impact of these uncertainties on their designs directly.

The foundation provided by full waveform metrology can now be leveraged and applied to today's waveform measurement problems [133, 134] and waveform measurement instrumentation. We conclude with a list of some potential problems and improvements.

#### 3.1. Connector-less on-wafer measurements

The trend away from modular components that are connected by coaxial cables or rectangular waveguide and towards increased system integration at the integrated circuit level has been a standard motivator for connector-less on-wafer measurements for many years. The recent demand for highly-efficient mm-wave systems is a new driver. Consider a power amplifier designed for mobile applications in the 60 GHz band. In order to design a high-efficiency amplifier, the designer must characterize the transistor performance up to at least the second and third harmonics at 120 GHz and 180 GHz respectively. For example, see [135–137]. LSNAs and other waveform measurement instruments are limited by the highest frequency of single-mode operation of the connectors between the the measurement system and the circuit being tested; i.e. 110 GHz for 1.0 mm and 145 GHz for 0.8 mm.

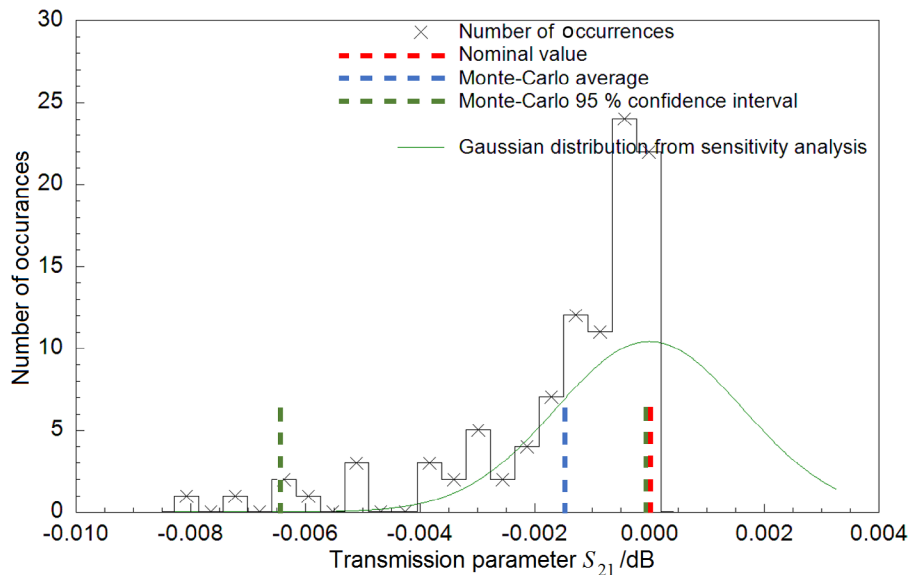


**Figure 10.** Uncertainty in the magnitude of the transfer function  $S_{21}$  of a passive junction between two rectangular waveguides. For details, see section 2.5.4.

Only microfabricated transmission lines and the smallest coaxial cables (for which no standard connectors are available) can support such bandwidths. Hence, there is a need for moving the measurement instrument *into* the wafer probe and thereby eliminating the need for connectors. Such instruments will require on-wafer standards and electro-optic sampling will undoubtedly play a role in calibrating instruments that are embedded in probes [88].

### 3.2. Connector-less radiated measurements

Fifth-generation wireless systems operating at mm-wave frequencies will require new over-the-air (OTA) test methods, both for evaluating the user equipment and for the base station [138, 139]. Some form of known free-field modulated signal will likely be needed to distinguish between the effects due to unintentional impairments in the measurement system and intentional channel effects. Reference modulated fields, based on calibrated signals at a coaxial reference plane [39], can be used to characterize the test system, assess the OTA test methods, and eliminate ambiguities regarding the origin of various measured impairments [133].

Because of the high propagation losses at mm-wave frequencies, fifth generation wireless systems will also need multiple antenna arrays to improve the effective antenna gain. This will be achieved through beam steering and signal processing that makes use of multiple input/multiple output (MIMO) antenna arrays [140, 141].

These low-cost antenna arrays will have active array elements and be highly integrated, compact, and low cost, with poor isolation between the elements. This will lead to several measurement and design challenges. First, the signal distortion will need to be measured in the presence of multiple interfering signals on the same antennas. Because the antennas will be poorly isolated, leakage from adjacent antennas will saturate the amplifiers that drive each antenna. This saturation will depend on the direction in which the transmitted beam

is pointed and the particular signals that are on each antenna [137, 142]. Free-field, modulated-signal measurements will be needed to characterize the effectiveness of various non-linear compensation strategies. Because the arrays are highly integrated, they may not have input connectors, so on-wafer probing strategies may need to be incorporated with the free-field measurements.

### 3.3. Time interleaved instruments

High-speed digitizers and real-time oscilloscopes (RTOs)<sup>8</sup> are typically used for capturing low-probability events, randomly varying signals, or one-time events. Examples include glitches in digital data streams, wireless signals over a fading channel and the shock wave from an explosion. RTOs often have sophisticated, software assisted trigger functionality for detecting very specific events, particularly for digital data streams. Some RTOs have large memory depth and can perform complicated signal processing, such as calculating error vector magnitude and displaying constellation patterns in real time. Both equivalent-time oscilloscopes and RTOs are now available with approximately 100 GHz bandwidth. A description of the architecture of real-time and equivalent-time oscilloscopes and their application to characterizing serial data interconnects can be found in [107].

From the perspective of a metrology lab, not associated with the manufacturer, RTOs pose a more complicated calibration problem than do equivalent-time oscilloscopes. This is because equivalent-time oscilloscopes use one sampler per input channel and one timebase for the entire mainframe. RTOs, with roughly 500 MHz or more bandwidth, interleave  $N$  analog to digital converters (ADCs), where  $N$  can be anywhere between 2 and a few hundred, depending on the oscilloscope bandwidth and manufacturer. Thus, when the aggregate

<sup>8</sup> For simplicity, we refer to both here as RTOs.

acquisition rate is  $f_s$ , the acquisition rate of any given ADC is  $f_s/N$ .

In an RTO, a master clock is distributed through  $N$  delay lines to each of the ADCs to control when each ADC makes a measurement. Due to manufacturing tolerances, the delay of each line usually must be trimmed to make the time interval between each ADC measurement acceptably close to  $f_s^{-1}$ . However, errors are always present in this trimming process, giving rise to periodic timing errors. Furthermore, each ADC, and the RF path to that ADC, has its own unique errors, both linear and nonlinear. Depending on the RTO manufacturer and the desired level of accuracy, the calibration model can be quite complicated and can contain nonlinear and non-time invariant aspects.

Some progress toward a metrology grade calibration has been made recently [143–145]. To the best of our knowledge, a time/frequency consistent uncertainty analysis for RTO measurements over several gigahertz of bandwidth is not currently available.

**3.3.1. Instrumentation nonlinearity.** We have observed significant nonlinearities in equivalent-time oscilloscopes, RTOs and LSNAs. Calibration of these nonlinearities could significantly enhance the dynamic range of these instruments and uncertainty analysis of their measurements.

## Acknowledgments

We thank NIST management, especially William Anderson, Kent Rochford, and Marla Dowell, for their early support of this work. This work is a contribution of the National Institute of Standards and Technology and is not subject to copywrite in the United States.

## ORCID iDs

Paul D Hale  <https://orcid.org/0000-0002-8791-6622>

## References

- [1] Optical interfaces for equipments, systems relating to the synchronous digital hierarchy CCITT (now ITU-T) recommendation G.957, Geneva, Switzerland, 1990
- [2] 1997 IEEE standard for wireless LAN medium access control (MAC) and physical layer (PHY) specifications IEEE Std 802.11-1997 (New York: IEEE) pp 1–445
- [3] Hale P D, Wang C M, Park R and Lau W Y 1996 A transfer standard for measuring photoreceiver frequency response *J. Lightwave Technol.* **14** 2457–66
- [4] Kahrs M 2003 50 years of RF and microwave sampling *IEEE Trans. Microw. Theory Technol.* **51** 1787–805
- [5] Blue K J, Cutler R T, O'Brian D P, Wagner D R and Zerlingo B R 1993 Vector signal analyzers for difficult measurements on time-varying and complex modulated signals *Hewlett-Packard J.* **44** 6–16
- [6] Moer W V and Gomme L 2010 NVNA versus LSNA: enemies or friends? *IEEE Microw. Mag.* **11** 97–103
- [7] Verspecht J 2005 Large-signal network analysis *IEEE Microw. Mag.* **6** 82–92
- [8] Marks R and Williams D F 1992 A general waveguide circuit theory *J. Res. Natl. Inst. Stand. Technol.* **97** 533–62
- [9] Kerns D M and Beatty R W 1967 *Basic Theory of Waveguide Junctions and Introductory Microwave Network Analysis* (Oxford: Pergamon)
- [10] Rush K, Draving S and Kerley J 1990 Characterizing high-speed oscilloscopes *IEEE Spectr.* **27** 38–9
- [11] Verspecht J and Rush K 1994 Individual characterization of broadband sampling oscilloscopes with a 'nose-to-nose' calibration procedure *IEEE Trans. Instrum. Meas.* **43** 347–54
- [12] Verspecht J 1995 Broadband sampling oscilloscope characterization with the 'nose-to-nose' calibration procedure: a theoretical and practical analysis *IEEE Trans. Instrum. Meas.* **44** 991–7
- [13] Verspecht J 1994 Compensation of timing jitter-induced distortion of sampled waveforms *IEEE Trans. Instrum. Meas.* **43** 726–32
- [14] Verspecht J 1994 Accurate spectral estimation based on measurements with a distorted-timebase digitizer *IEEE Trans. Instrum. Meas.* **43** 210–5
- [15] DeGroot D C, Hale P D, vanden Bossche M, Verbeyst F and Verspecht J 2000 Analysis of interconnection networks and mismatch in the nose-to-nose calibration *55th ARFTG Conf. Digest* vol 37 pp 1–6
- [16] Scott W R and Smith G S 1986 Error corrections for an automated time-domain network analyzer *IEEE Trans. Instrum. Meas.* **IM-35** 300–3
- [17] Nahman N S 1989 Reference pulse generators: theory, application, and status of development *IEEE Trans. Instrum. Meas.* **38** 442–7
- [18] Gans W L 1990 Dynamic calibration of waveform recorders and oscilloscopes using pulse standards *IEEE Trans. Instrum. Meas.* **39** 952–7
- [19] 2011 IEEE standard for transitions, pulses, and related waveforms IEEE Std 181-2011 (Revision of IEEE Std 181-2003) (New York: IEEE)
- [20] Füser H, Eichstädt S, Baaske K, Elster C, Kuhlmann K, Judaschke R, Pierz K and Bieler M 2012 Optoelectronic time-domain characterization of a 100 GHz sampling oscilloscope *Meas. Sci. Technol.* **23** 025201
- [21] Dienstfrey A and Hale P D 2014 Analysis for dynamic metrology *Meas. Sci. Technol.* **25** 035001
- [22] Stone J A 2009 Uncalibrated helium–neon lasers in length metrology *NCSLI Meas.* **4** 52–8
- [23] Dienstfrey A, Hale P D, Keenan D A, Clement T S and Williams D F 2006 Minimum-phase calibration of sampling oscilloscopes *IEEE Trans. Microw. Theory Technol.* **54** 3197–208
- [24] Cui X and Crowley T P 2011 Comparison of experimental techniques for evaluating the correction factor of a rectangular waveguide microcalorimeter *IEEE Trans. Instrum. Meas.* **60** 2690–5
- [25] Wallis T M, Crowley T P, LeGolvan D X and Ginley R A 2012 A direct comparison system for power calibration up to 67 GHz *2012 Conf. on Precision electromagnetic Measurements* pp 726–7
- [26] Daywitt W C 1991 Exact principal mode field for a lossy coaxial line *IEEE Trans. Microw. Theory Technol.* **39** 1313–22
- [27] Daywitt W C 1995 The propagation constant of a lossy coaxial line with a thick outer conductor *IEEE Trans. Microw. Theory Technol.* **43** 907–11
- [28] Leuchtmann P and Rufenacht J 2004 On the calculation of the electrical properties of precision coaxial lines *IEEE Trans. Instrum. Meas.* **53** 392–7
- [29] Horibe M, Shida M and Komiyama K 2009 Development of evaluation techniques for air lines in 3.5 and 1.0 mm line sizes *IEEE Trans. Instrum. Meas.* **58** 1078–83

- [30] Zeier M, Hoffmann J, Hrlimann P, Rfenacht J, Stalder D and Wollensack M 2018 Establishing traceability for the measurement of scattering parameters in coaxial line systems *Metrologia* **55** S23
- [31] Marks R B and Williams D F 1991 Characteristic impedance determination using propagation constant measurement *IEEE Microw. Guid. Wave Lett.* **1** 141–3
- [32] Williams D F and Marks R B 1991 Transmission line capacitance measurement *IEEE Microw. Guid. Wave Lett.* **1** 243–5
- [33] Parker T E, Jefferts S R and Heavner T P 2010 Medium-term frequency stability of hydrogen masers as measured by a cesium fountain 2010 *IEEE Int. Frequency Control Symp.* pp 318–23
- [34] Hale P D, Wang C M, Williams D F, Remley K A and Wepman J D 2006 Compensation of random and systematic timing errors in sampling oscilloscopes *IEEE Trans. Instrum. Meas.* **55** 2146–54
- [35] Wang C M, Hale P D and Williams D F 2009 Uncertainty of timebase corrections *IEEE Trans. Instrum. Meas.* **58** 3468–72
- [36] Wang C M J, Hale P D, Jargon J A, Williams D F and Remley K A 2012 Sequential estimation of timebase corrections for an arbitrarily long waveform *IEEE Trans. Instrum. Meas.* **61** 2689–94
- [37] Reader H C, Williams D F, Hale P D and Clement T S 2008 Comb-generator characterization *IEEE Trans. Microw. Theory Technol.* **56** 515–21
- [38] Hale P D, Dienstfrey A, Wang J C M, Williams D F, Lewandowski A, Keenan D A and Clement T S 2009 Traceable waveform calibration with a covariance-based uncertainty analysis *IEEE Trans. Instrum. Meas.* **58** 3554–68
- [39] Remley K A, Williams D F, Hale P D, Wang C M, Jargon J and Park Y 2015 Millimeter-wave modulated-signal and error-vector-magnitude measurement with uncertainty *IEEE Trans. Microw. Theory Technol.* **63** 1710–20
- [40] Cox M, Dainton M, Harris P and Ridler N 1999 The evaluation of uncertainties in the analysis of calibration data In *Proc. of the 16th IEEE Instrumentation and Measurement Technology Conf. (Cat. No.99CH36309)* vol 2 pp 1093–8
- [41] Ridler N M and Salter M J 2002 An approach to the treatment of uncertainty in complex s-parameter measurements *Metrologia* **39** 295
- [42] Hale P D and Wang C M J 2009 Calculation of pulse parameters and propagation of uncertainty *IEEE Trans. Instrum. Meas.* **58** 639–48
- [43] Eichstädt S, Wilkens V, Dienstfrey A, Hale P, Hughes B and Jarvis C 2016 On challenges in the uncertainty evaluation for time-dependent measurements *Metrologia* **53** S125
- [44] Nahman N S 1978 Picosecond-domain waveform measurements *Proc. IEEE* **66** 441–54
- [45] Nahman N S 1983 Picosecond-domain waveform measurement: Status and future directions *IEEE Trans. Instrum. Meas.* **32** 117–24
- [46] Lawton R A, Riad S M and Andrews J R 1986 Pulse and time-domain measurements *Proc. IEEE* **74** 77–81
- [47] Harper M R, Smith A J A, Basu A and Humphreys D A 2004 Calibration of a 70 GHz oscilloscope *Conf. on Precision Electromagnetic Measurements* pp 530–1
- [48] Bieler M, Seitz S, Spitzer M, Hein G, Pierz K, Siegner U, Basu M A, Smith A J A and Harper M R 2007 Rise-time calibration of 50 GHz sampling oscilloscopes: Intercomparison between PTB and NPL *IEEE Trans. Instrum. Meas.* **56** 266–70
- [49] Henderson D, Roddie A G and Smith A J A 1992 Recent developments in the calibration of fast sampling oscilloscopes *IEE Proc. A* **139** 254–60
- [50] Deyst J P, Paulter N G, Daboczi T, Stenbakken G N and Souders T M 1998 A fast-pulse oscilloscope calibration system *IEEE Trans. Instrum. Meas.* **47** 1037–41
- [51] Riad S M 1982 Modeling of the HP-1430A feedthrough wide-band (28 ps) sampling head *IEEE Trans. Instrum. Meas.* **IM-31** 110–5
- [52] Hale P D, Clement T S, Coakley K J, Wang C M, DeGroot D C and Verdoni A P 2000 Estimating the magnitude and phase response of a 50 GHz sampling oscilloscope using the ‘nose-to-nose’ method *55th ARFTG Conf. Digest* vol 37 pp 1–8
- [53] Larson D R and Paulter N G 2001 Using the nose-to-nose sampler calibration method in pulse metrology *11th IMEKO TC-4 Symp.*
- [54] Remley K A 2003 The impact of internal sampling circuitry on the phase error of the nose-to-nose oscilloscope calibration *National Institute of Standards and Technology, NIST TN-1528*
- [55] Paulter N G and Larson D R 2003 Sources of uncertainty in the nose-to-nose sampler calibration method *IEEE Trans. Instrum. Meas.* **52** 1618–26
- [56] Scott J B 2003 Rapid millimetre-wave sampler response characterization to well beyond 120 GHz using an improved nose-to-nose method *IEEE MTT-S Int. Microwave Symp. Digest* vol 3 pp 1511–4
- [57] Clement T S, Hale P D, Williams D F, Wang C M, Dienstfrey A and Keenan D A 2006 Calibration of sampling oscilloscopes with high-speed photodiodes *IEEE Trans. Microw. Theory Technol.* **54** 3173–81
- [58] Bieler M, Spitzer M, Pierz K and Siegner U 2009 Improved optoelectronic technique for the time-domain characterization of sampling oscilloscopes *IEEE Trans. Instrum. Meas.* **58** 1065–71
- [59] Boaventura A J S, Williams D, Avolio G and Hale P 2018 Traceable characterization of broadband pulse waveforms using a large signal network analyzer and a sampling oscilloscope *IEEE MTT-S Int. Microwave Symp. Digest*
- [60] Williams D F and Remley K A 2001 Analytic sampling-circuit model *IEEE Trans. Microw. Theory Technol.* **49** 1013–9
- [61] Remley K A, Williams D F, DeGroot D C, Verspecht J and Kerley J 2001 Effects of nonlinear diode junction capacitance on the nose-to-nose calibration *IEEE Microw. Wirel. Compon. Lett.* **11** 196–8
- [62] Williams D F, Clement T S, Remley K A, Hale P D and Verbeyst F 2007 Systematic error of the nose-to-nose sampling-oscilloscope calibration *IEEE Trans. Microw. Theory Technol.* **55** 1951–7
- [63] Lee C H (ed) 1984 *Picosecond Optoelectronic Devices* (New York: Academic)
- [64] Auston D H 1993 Ultrafast optoelectronics *Ultrashort laser pulses: Generation and applications* ed W Kaiser (Berlin: Springer) vol 60 ch 5
- [65] Kolner B and Bloom D 1986 Electrooptic sampling in GaAs integrated circuits *IEEE J. Quantum Electron.* **22** 79–93
- [66] Weingarten K J, Majidi-Ahy R, Rodwell M J W, Auld B A and Bloom D M 1987 Microwave measurements of GaAs integrated circuits using electrooptic sampling *1987 IEEE MTT-S Int. Microw. Symp. Digest* vol 2 pp 877–80
- [67] Valdmanis J and Mourou G 1986 Subpicosecond electrooptic sampling: Principles and applications *IEEE J. Quantum Electron.* **22** 69–78
- [68] Seitz S, Bieler M, Hein G, Pierz K, Siegner U, Schmckle F J and Heinrich W 2006 Characterization of an external electro-optic sampling probe: influence of probe height on distortion of measured voltage pulses *J. Appl. Phys.* **100** 113124
- [69] Seitz S, Bieler M, Hein G, Pierz K, Siegner U, Schmckle F J and Heinrich W 2007 Correction of picosecond voltage

- pulses measured with external electro-optic sampling tips *Meas. Sci. Technol.* **18** 1353
- [70] Lee D-J, Kwon J-Y and Kang N-W 2014 Field analysis of electro-optic probes for minimally invasive microwave sampling *Opt. Express* **22** 2897–909
- [71] Williams D F, Hale P D, Clement T S and Morgan J M 2000 Mismatch corrections for electro-optic sampling systems In *56th ARFTG Conference Digest* vol **38** pp 1–5
- [72] Bieler M, Füsler H and Pierz K 2015 Time-domain optoelectronic vector network analysis on coplanar waveguides *IEEE Trans. Microw. Theory Technol.* **63** 3775–84
- [73] Yariv A and Yeh P 1984 *Optical Waves in Crystals* (New York: Wiley-Interscience)
- [74] Clement T S, Williams D F, Hale P D and Morgan J M 2002 Calibrating photoreceiver response to 110 GHz *The 15th Annual Meeting of the IEEE Lasers and Electro-Optics Society* vol 2 pp 877–8
- [75] Williams D F, Hale P D, Clement T S and Morgan J M 2001 Calibrating electro-optic sampling systems *IEEE MTT-S Int. Microw. Symp. Digest (Cat. No.01CH37157)* vol 3 pp 1527–30
- [76] Williams D, Hale P, Clement T and Wang C-M 2004 Uncertainty of the NIST electrooptic sampling system *National Institute of Standards and Technology, NIST TN-1535*
- [77] Diels J-C and Rudolph W 1996 *Ultrashort Laser Pulse Phenomena* (New York: Academic)
- [78] Hale P D and Williams D F 2003 Calibrated measurement of optoelectronic frequency response *IEEE Trans. Microw. Theory Technol.* **51** 1422–9
- [79] Bottacchi S, Beling A, Matiss A, Nielsen M L, Steffan A G, Unterbrsch G and Umbach A 2010 Advanced photoreceivers for high-speed optical fiber transmission systems *IEEE J. Sel. Top. Quantum Electron.* **16** 1099–112
- [80] Ito H, Kodama S, Muramoto Y, Furuta T, Nagatsuma T and Ishibashi T 2004 High-speed and high-output InP–InGaAs untraveling-carrier photodiodes *IEEE J. Sel. Top. Quantum Electron.* **10** 709–27
- [81] Shimizu N, Watanabe N, Furuta T and Ishibashi T 1998 Inp-ingaas uni-traveling-carrier photodiode with improved 3-db bandwidth of over 150 GHz *IEEE Photonics Technol. Lett.* **10** 412–4
- [82] Liu P-L, Williams K J, Frankel M Y and Esman R D 1999 Saturation characteristics of fast photodetectors *IEEE Trans. Microw. Theory Technol.* **47** 1297–303
- [83] Hale P D, Clement T S, Williams D F, Balta E and Taneja N D 2001 Measuring the frequency response of gigabit chip photodiodes *J. Lightwave Technol.* **19** 1333–9
- [84] Williams D F and Alpert B K 2001 Causality and waveguide circuit theory *IEEE Trans. Microw. Theory Technol.* **49** 615–23
- [85] Williams D 2013 Traveling waves and power waves: building a solid foundation for microwave circuit theory *IEEE Microw. Mag.* **14** 38–45
- [86] 1972 S-parameter design Hewlett Packard Application Note 154 (USA)
- [87] Paulter N G, Smith A J A, Larson D R, Souders T M and Roddie A G 2003 NIST-NPL interlaboratory pulse measurement comparison *IEEE Trans. Instrum. Meas.* **52** 1825–33
- [88] Williams D F, Hale P D, Clement T S and Morgan J M 2005 Calibrated 200 GHz waveform measurement *IEEE Trans. Microw. Theory Technol.* **53** 1384–9
- [89] Williams D F, Lewandowski A, Clement T S, Wang J C M, Hale P D, Morgan J M, Keenan D A and Dienstfrey A 2006 Covariance-based uncertainty analysis of the NIST electrooptic sampling system *IEEE Trans. Microw. Theory Technol.* **54** 481–91
- [90] Williams D, Clement T, Hale P and Dienstfrey A 2006 Terminology for high-speed sampling-oscilloscope calibration *68th ARFTG Conf. Digest*
- [91] Lewandowski A, Williams D F, Hale P D, Wang J C M and Dienstfrey A 2010 Covariance-based vector-network-analyzer uncertainty analysis for time- and frequency-domain measurements *IEEE Trans. Microw. Theory Technol.* **58** 1877–86
- [92] Williams D F and Marks R B 1992 Calibrating on-wafer probes to the probe tips *40th ARFTG Conf. Digest* vol 22 pp 136–43
- [93] Kaiser R F and Williams D F 1999 Sources of error in coplanar-waveguide trl calibrations *54th ARFTG Conf. Digest* vol 36 pp 1–6
- [94] Williams D F, Wang J C M and Arz U 2003 An optimal vector-network-analyzer calibration algorithm *IEEE Trans. Microw. Theory Technol.* **51** 2391–401
- [95] Williams D F, Jamroz B and Lewandowski A 2018 NIST microwave uncertainty framework Beta version ([www.nist.gov/services-resources/software/wafer-calibration-software](http://www.nist.gov/services-resources/software/wafer-calibration-software))
- [96] Williams D F, Schmckle F J, Doerner R, Phung G N, Arz U and Heinrich W 2014 Crosstalk corrections for coplanar-waveguide scattering-parameter calibrations *IEEE Trans. Microw. Theory Technol.* **62** 1748–61
- [97] Probst T, Doerner R, Ohlrogge M, Lozar R and Arz U 2017 110 GHz on-wafer measurement comparison on alumina substrate *2017 90th ARFTG Microwave Measurement Symp. (ARFTG)* pp 1–4
- [98] Arz U, Zinal S, Probst T, Hechtfisher G, Schmckle F J and Heinrich W 2017 Establishing traceability for on-wafer s-parameter measurements of membrane technology devices up to 110 GHz *2017 90th ARFTG Microwave Measurement Symp. (ARFTG)* pp 1–4
- [99] Schmckle F J, Probst T, Arz U, Phung G N, Doerner R and Heinrich W 2017 Mutual interference in calibration line configurations *2017 89th ARFTG Microwave Measurement Conf. (ARFTG)* pp 1–4
- [100] Bieler M and Arz U 2016 Characterization of high-frequency interconnects: comparison between time- and frequency-domain methods *2016 IEEE 20th Workshop on Signal and Power Integrity (SPI)* pp 1–4
- [101] Struszewski P, Pierz K and Bieler M 2017 Time-domain characterization of high-speed photodetectors *J. Infrared Millim. Terahertz Waves* **38** 1416–31
- [102] Hale P D, Williams D F, Dienstfrey A, Wang J, Jargon J, Humphreys D, Harper M, Füsler H and Bieler M 2012 Traceability of high-speed electrical waveforms at NIST, NPL, and PTB *2012 Conf. on Precision electromagnetic Measurements* pp 522–3
- [103] Papoulis A 1962 *The Fourier Integral and Its Applications* (New York: McGraw-Hill)
- [104] Hansen P 1998 *Rank-Deficient and Discrete Ill-Posed Problems* (Philadelphia, PA: Society for Industrial and Applied Mathematics)
- [105] Vogel C 2002 *Computational Methods for Inverse Problems* (Philadelphia, PA: Society for Industrial and Applied Mathematics)
- [106] Dienstfrey A and Hale P D 2014 Colored noise and regularization parameter selection for waveform metrology *IEEE Trans. Instrum. Meas.* **63** 1769–78
- [107] Derickson D and Müller M 2007 *Digital Communications Test and Measurement: High-speed Physical Layer Characterization* 1st edn ( Boston, MA: Prentice Hall)
- [108] Stenbakken G N and Deyst J P 1998 Time-base nonlinearity determination using iterated sine-fit analysis *IEEE Trans. Instrum. Meas.* **47** 1056–61
- [109] Wang C M, Hale P D and Coakley K J 1999 Least-squares estimation of time-base distortion of sampling oscilloscopes *IEEE Trans. Instrum. Meas.* **48** 1324–32

- [110] Humphreys D and Akmal M 2012 Channel timebase errors for digital sampling oscilloscopes *2012 Conf. on Precision Electromagnetic Measurements* pp 520–1
- [111] Vandersteen G, Rolain Y and Schoukens J 2001 An identification technique for data acquisition characterization in the presence of nonlinear distortions and time base distortions *IEEE Trans. Instrum. Meas.* **50** 1355–63
- [112] Jargon J A, Hale P D and Wang C M 2010 Correcting sampling oscilloscope timebase errors with a passively mode-locked laser phase locked to a microwave oscillator *IEEE Trans. Instrum. Meas.* **59** 916–22
- [113] Coakley K J and Hale P 2001 Alignment of noisy signals *IEEE Trans. Instrum. Meas.* **50** 141–9
- [114] Verbeyst F, Pintelon R, Rolain Y, Schoukens J and Clement T S 2007 System identification approach applied to drift estimation In *2007 IEEE Instrumentation Measurement Technology Conf.* pp 1–6
- [115] Humphreys D A, Harris P M, Rodriguez-Higuero M, Mubarak F A, Zhao D and Ojasalo K 2015 Principal component compression method for covariance matrices used for uncertainty propagation *IEEE Trans. Instrum. Meas.* **64** 356–65
- [116] Remley K A, Williams D F, Schreurs D M M P, Loglio G and Cidronali A 2003 Phase detrending for measured multisine signals *61st ARFTG Conf. Digest, Spring* pp 73–83
- [117] Ma Z, Ma H, Gong P, Yang C and Feng K 2010 Ultrafast optoelectronic technology for radio metrology applications *J. Syst. Eng. Electron.* **21** 461–8
- [118] Gong P, Xie W, Chen B, Jiang H, Ma H, Yang C and Wen S 2016 Traceability of ultrafast electrical pulse waveforms at BIRMM *41st Int. Conf. on Infrared, Millimeter, and Terahertz waves (IRMMW-THz)* pp 1–2
- [119] Li J W, Xu N, Li J and Zhang Z X 2012 Ultrafast electrical signal electro-optic sampling test theory and test system *Opto-Electronics Engineering and Materials Research (Advanced Materials Research vol 571)* pp 471–5 (*Trans. Technol. Publ.* 10)
- [120] Li A J, Gan B H and Xu C N 2015 Test system of 100 GHz photodetector time response at NIM *11th Conf. on Lasers and Electro-Optics Pacific Rim (CLEO-PR)* vol 1 pp 1–2
- [121] Feng Z, Zhao K, Yang Z, Miao J and Chen H 2018 100 GHz pulse waveform measurement based on electro-optic sampling *Laser Phys.* **28** 055301
- [122] Lin M and Zhang Y 2012 Covariance-matrix-based uncertainty analysis for NVNA measurements *IEEE Trans. Instrum. Meas.* **61** 93–102
- [123] Ojasalo K, Hudlička M and Humphreys D A 2014 Uncertainty of communication signals measurement *29th Conf. on Precision Electromagnetic Measurements (CPEM 2014)* pp 338–9
- [124] Zhang Y, Guo X, He Z, Huang H, Huang J, Nie M, Wang L, Yang A and Lu Z 2016 Characterization for multiharmonic intermodulation nonlinearity of RF power amplifiers using a calibrated nonlinear vector network analyzer *IEEE Trans. Microw. Theory Technol.* **64** 2912–23
- [125] Eichstädt S, Elster C, Smith I M and Esward T J 2017 Evaluation of dynamic measurement uncertainty—an open-source software package to bridge theory and practice *J. Sens. Syst.* **6** 97–105
- [126] Eichstädt S and Wilkens V 2016 GUM2DFT—a software tool for uncertainty evaluation of transient signals in the frequency domain *Meas. Sci. Technol.* **27** 055001
- [127] Garelli M and Ferrero A 2012 A unified theory for s-parameter uncertainty evaluation *IEEE Trans. Microw. Theory Technol.* **60** 3844–55
- [128] Wollensack M, Hoffmann J, Ruefenacht J and Zeier M 2012 VNA tools ii: S-parameter uncertainty calculation *79th ARFTG Conf. Digest*
- [129] Avolio G, Williams D F, Streett S, Frey M, Schreurs D, Ferrero A and Dieudonn M 2017 Software tools for uncertainty evaluation in VNA measurements: a comparative study *2017 89th ARFTG Microwave Measurement Conf. (ARFTG)* pp 1–7
- [130] Avolio G, Raffo A, Jargon J, Hale P D, Schreurs D M M P and Williams D F 2015 Evaluation of uncertainty in temporal waveforms of microwave transistors *IEEE Trans. Microw. Theory Technol.* **63** 2353–63
- [131] Williams D F, Chamberlin R A, Zhao W, Cheron J and Urteaga M E 2016 Transistor model verification including measurement uncertainty *IEEE Trans. Microw. Theory Technol.* **64** 3927–33
- [132] Cheron J and Williams D 2018 Measurement uncertainty for compact modeling and mmwave circuit design *11th Global Symp. on Millimeter Waves (GSMM) 2018 Conf. Digest*
- [133] Remley K A et al 2017 Measurement challenges for 5G and beyond: an update from the National Institute of Standards and Technology *IEEE Microw. Mag.* **18** 41–56
- [134] Humphreys D A, Fatadin I, Bieler M, Struszewski P and Hudlička M 2017 Optical and RF metrology for 5G *2017 IEEE Photonics Society Summer Topical Meeting Series (SUM)* pp 195–6
- [135] Tasker P J 2009 Practical waveform engineering *IEEE Microw. Mag.* **10** 65–76
- [136] Datta K and Hashemi H 2014 Performance limits, design and implementation of mm-wave sige HBT Class-E and stacked Class-E power amplifiers *IEEE J. Solid-State Circuits* **49** 2150–71
- [137] Bassam S A, Helaoui M and Ghannouchi F M 2009 Crossover digital predistorter for the compensation of crosstalk and nonlinearity in MIMO transmitters *IEEE Trans. Microw. Theory Technol.* **57** 1119–28
- [138] Qi Y, Yang G, Liu L, Fan J, Orlandi A, Kong H, Yu W and Yang Z 2017 5G over-the-air measurement challenges: overview *IEEE Trans. Electromagn. Compat.* **59** 1661–70
- [139] Rumney M 2016 Testing 5G: time to throw away the cables *Microw. J.* **59** 1661–70
- [140] Roh W, Seol J Y, Park J, Lee B, Lee J, Kim Y, Cho J, Cheun K and Aryanfar F 2014 Millimeter-wave beamforming as an enabling technology for 5G cellular communications: theoretical feasibility and prototype results *IEEE Commun. Mag.* **52** 106–13
- [141] Swindlehurst A L, Ayanoglu E, Heydari P and Capolino F 2014 Millimeter-wave massive MIMO: the next wireless revolution? *IEEE Commun. Mag.* **52** 56–62
- [142] Hausmair K, Gustafsson S, Sanchez-Prez C, Landin P N, Gustavsson U, Eriksson T and Fager C 2017 Prediction of nonlinear distortion in wideband active antenna arrays *IEEE Trans. Microw. Theory Technol.* **65** 4550–63
- [143] Humphreys D A, Hudlička M and Fatadin I 2015 Calibration of wideband digital real-time oscilloscopes *IEEE Trans. Instrum. Meas.* **64** 1716–25
- [144] Cho C, Lee J G, Hale P D, Jargon J A, Jeavons P, Schlager J B and Dienstfrey A 2016 Calibration of time-interleaved errors in digital real-time oscilloscopes *IEEE Trans. Microw. Theory Technol.* **64** 4071–79
- [145] Kim D, Lee J-G, Lee D-J and Cho C 2018 Traceable calibration for a digital real-time oscilloscope with time interleaving architecture *Meas. Sci. Technol.* **29** 015003